ACS APPLIED ENERGY MATERIALS

www.acsaem.org
Article

Tetrabenzonaphthalene and Redox-Active Anthraquinone-Linked Conjugated Microporous Polymers as Organic Electrodes for Enhanced Energy Storage Efficiency

Mohamed Gamal Mohamed,*,⊥ Mervat Ibrahim,⊥ Nian Ping Chen, Abdul Basit, Yang Chin Kao, Aya Osama Mousa, Maha Mohamed Samy, and Shiao-Wei Kuo*

Cite This: ACS Appl. Energy Mater. 2024, 7, 5582−5593

Read Online

ACCESS | Metrics & More | Article Recommendations | Supporting Information

ABSTRACT: Various energy storage systems widely utilize conjugated microporous polymers (CMPs) due to their porous architecture and expansive surface area, which facilitate efficient ion transport and storage. In our research, we developed two anthraquinone (ATQ)-based CMPs (ATQ-CMPs) through a Sonogashira coupling method. We used 2,6-dibromoanthraquinone (ATQ-Br_2), a redox-active precursor, as a building monomer along with an ethynyl derivative of triphenylamine (TPA-T) and tetrabenzonaphthalene (TBN-T) to afford TPA-ATQ CMP and TBN-ATQ CMP, respectively. We employed techniques, such as thermogravimetric analysis, high-resolution transmission electron microscopy (HR-TEM), scanning electron microscopy (SEM), and Fourier-transform infrared spectroscopy (FTIR), to characterize the structure and thermal properties of these ATQ-CMPs. The TBN-ATQ CMP displayed extensive Brunauer−Emmett−Teller (BET) surface areas (S_{BET} = 161 m^2 g^{-1}) and remarkable thermal stability (temperatures of up to 605 °C). These properties made it an excellent candidate for supercapacitor (SC) electrode materials. The electrodes fabricated using the TBN-ATQ CMP exhibited an exceptionally significant specific capacitance of 393 F g^{-1} when tested at a current density of 1 A g^{-1}. After 5000 cycles at 10 A g^{-1}, TBN-ATQ CMP still had 74.2% capacitance in a three-electrode setup. We also made a symmetrical device using the TBN-ATQ CMP. This device had a capacitance of 175 F g^{-1} at 1 A g^{-1} and was very stable over 2000 cycles, keeping 92.8% of its capacitance. The TBN-ATQ CMP electrode has better electrochemical performance because it has a redox-active ATQ unit and high S_{BET}. Our findings pave the way for simple methods of developing and producing efficient CMP materials using TBN and ATQ for high-performance SCs in both three- and two-electrode configurations.

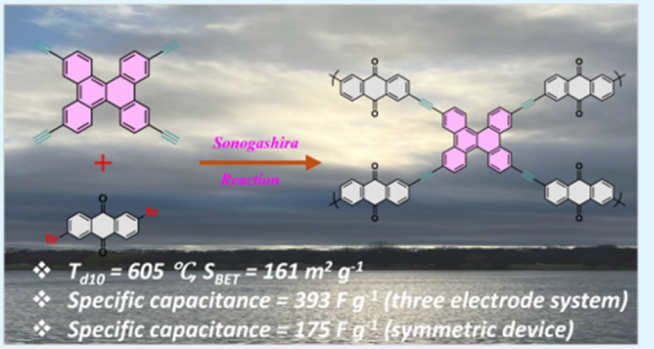

KEYWORDS: *tetrabenzonaphthalene, anthraquinone, redox-active unit, conjugated microporous polymers, thermal stability, supercapacitors*

INTRODUCTION

The growing concerns over pollution, climate change, and the depletion of fossil fuels are intensifying global energy and environmental issues.[1−10] These challenges have spurred significant efforts to develop advanced alternative energy storage systems to satisfy future energy demands.[1−10] Consequently, there is an increasing focus on technologies for wastewater, water, and wind energy management as well as for storing materials and converting renewable energy sources. However, several challenges impede the adoption of energy storage systems, including low energy density, inadequate safety protocols, and a limited lifespan. Advanced energy storage technologies are crucial as they can enhance energy efficiency, facilitate rapid energy absorption, and release, and support the consistent growth of renewable energy sources.[10−15] These technologies also play a pivotal role in balancing the energy supply and demand. In response to current energy challenges, there has been a marked surge in research focused on innovative technology-based solutions for energy storage and renewable energy.[16−20] In recent years, significant research has been directed toward developing energy storage systems that efficiently store electrical energy from renewable sources and deliver it on demand globally.[21−25] These systems are crucial for keeping pace with rapid technological advancements in sectors requiring high power

Received: May 17, 2024
Revised: June 7, 2024
Accepted: June 13, 2024
Published: June 22, 2024

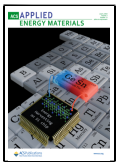

Scheme 1. Illustration Showcasing the Synthesis of (a) TPA-ATQ CMP and (b) TBN-ATQ CMP via Sonogashira Coupling

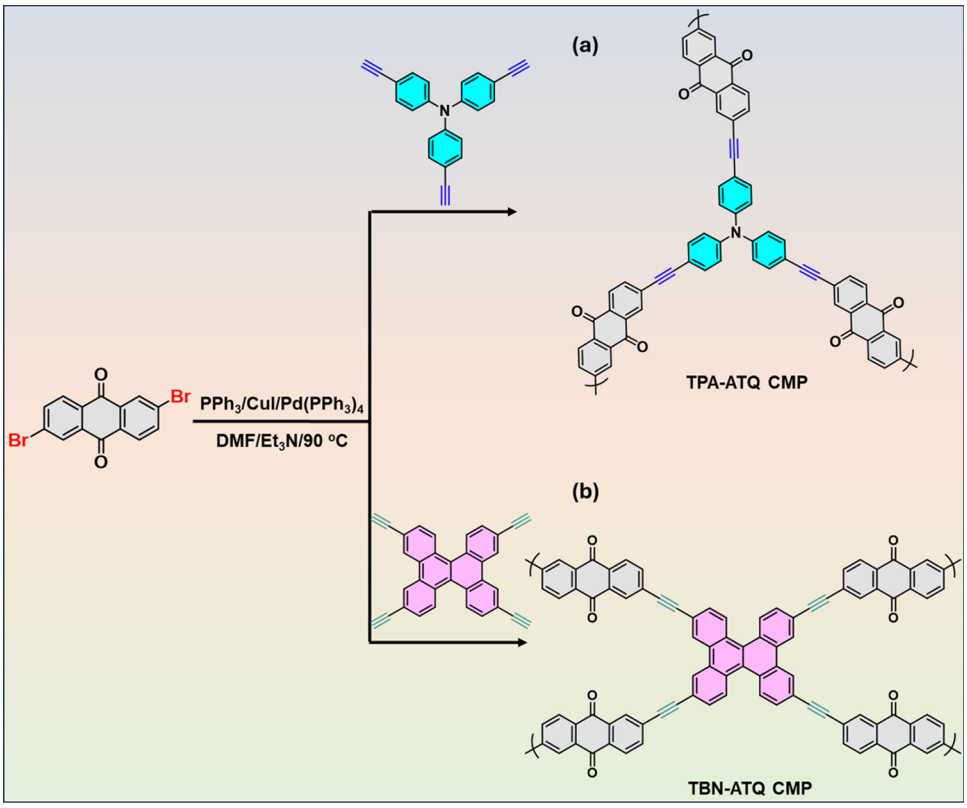

and energy density, such as electric vehicles and portable electronics. Supercapacitors (SCs), known for their high energy density, are emerging as one of the most promising electrochemical energy storage technologies. They are poised to replace conventional capacitors and batteries, offering substantial benefits for sustainable energy strategies and broader adoption in energy storage.[26−30] SCs are highly valued in various applications due to their rapid charge and discharge capabilities, long service life, and high operational efficiency. Among their many benefits, supercapacitors are particularly noted for their safety, superior electrochemical attributes, extended charge/discharge cycles, and environmental sustainability.[31−34]

Porous materials play a crucial role across various scientific and technological fields, attracting considerable attention for their potential to enhance functional material design.[35−39] conjugated microporous polymers (CMPs) represent a prominent category of organic porous polymers. They are distinguished by their high porosity, lightweight structure, and robust covalent bonds.[40−44] As a subset of covalently bonded organic porous materials, CMPs are amorphous and facilitate the conjugated assembly of building blocks within three-dimensional (3D) networks.[44−49] CMPs possess distinctive structural characteristics not found in other porous materials, which typically lack π-conjugation, or in conventional conjugated polymers, which are not porous.[44−49] CMPs leverage π-conjugated systems, allowing for deliberate modifications to their porous structures, thus enhancing both the framework and its properties.[44−49] CMPs can be synthesized through various chemical methods, including the Yamamoto reaction, Friedel−Crafts arylation, cyclotrimerization, Suzuki reaction, Sonogashira−Hagihara reaction, and Schiff base reaction, all of which contribute to the formation of these unique CMPs.[50−56] The design of CMPs allows for versatile applications. Primarily, they are utilized for their energy storage, photocatalytic H_2 production, chemical sensing, and biological applications.[40,41,54,56−60] However, significant challenges hinder the practical application of CMPs in electrochemical energy storage. The naturally low electrical conductivity of CMPs restricts charge transport within the frameworks, thereby limiting their electrochemical performance. To overcome this, we integrate redox-active components, such as anthraquinone (ATQ) moieties, into the frameworks to attain high theoretical capacities and enhance energy densities.[61,62] According to Huo et al., CC-DAQ-CMP has excellent stability with a capacitance of 184 F g^{-1}.[62]

In this work, we demonstrate the design and construction of new ATQ-CMPs (TPA-ATQ and TBN-ATQ CMPs), a unique CMP network composed of ATQ, TPA-T, and TBN-T monomers through the Sonogashira coupling process [Scheme 1]. Due to its high specific surface area, high thermal stability, large number of pores, and ATQ redox group, the TBN-ATQ CMP is a great supercapacitor for electrochemistry. In a three-electrode system, the TBN-ATQ CMP electrode demonstrated an excellent specific capacity of 393 F g^{-1} (1 A g^{-1}) and maintained 74.2% capacitance after 5000 cycles at 10 A g^{-1}. We also used the TBN-ATQ CMP to create a symmetrical device. This device, with a specific capacity of 175 F g^{-1} at 1 A g^{-1}, maintained 92.8% of its capacitance across 2000 cycles, demonstrating remarkable stability. Our research and results demonstrate that combining TBN and ATQ simplifies the production of CMP materials, facilitating the development of high-performance supercapacitors (SCs) suitable for configurations with either three or two electrodes.

https://doi.org/10.1021/acsaem.4c01276
ACS Appl. Energy Mater. 2024, 7, 5582−5593

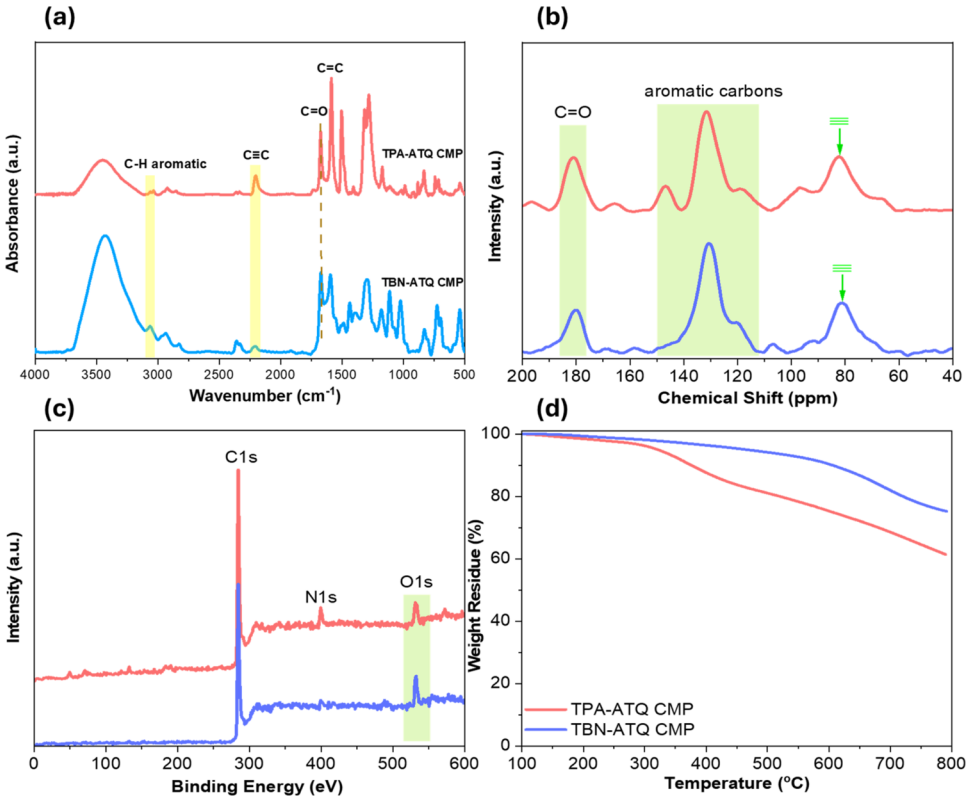

Figure 1. (a) FTIR, (b) ^{13}C CP/MAS NMR, (c) XPS, and (d) TGA profiles of TPA-ATQ CMP and TBN-ATQ CMP.

EXPERIMENTAL SECTION

Materials. Trimethylsilylacetylene (TMS, 98%), diethylamine (DEA, ≥99.5%), 2,6-diaminoanthraquinone (ATQ-2NH$_2$, 97%), triethylamine (Et$_3$N, ≥99.5%), acetonitrile (MeCN), copper(II) bromide (CuBr$_2$, 99%), copper(I) iodide (CuI, ≥99.5%), acetone, triphenylphosphine (PPh$_3$, 99%), potassium carbonate (K$_2$CO$_3$, ≥99.5%), methanol (MeOH), bis(triphenylphosphine)palladium(II) dichloride (PdCl$_2$(PPh$_3$)$_2$ 98%), and tetrakis(triphenylphosphine)-palladium [Pd(PPh$_3$)$_4$, 99%] were received from Sigma-Aldrich, Acros, and Alfa Aesar. We prepared TPA-Br$_3$ and TBN-Br$_4$, using our previously published protocol.[52,63,64] The Supporting Information file includes detailed procedures for synthesizing TBN-TMS and TBN-T, along with their Fourier-transform infrared (FTIR) and nuclear magnetic resonance (NMR) spectroscopy data [Schemes S1, S2 and Figures S1−S6].[22]

Synthesis of 2,6-Dibromoanthraquinone (ATQ-Br$_2$).[65] A mixture comprising CuBr$_2$ (14.08 g, 63.00 mmol) and ATQ-2NH$_2$ (6.00 g, 25.2 mmol) dissolved in MeCN (200 mL) was supplemented with 24 mL of *tert*-butyl nitrite in a dried reaction flask. After 24 h of reflux at 75 °C, 400 mL of 6 M HCl was incrementally introduced. The filtered yield of brown powder underwent sequential washing with water, MeCN, and MeOH, ultimately granting ATQ-Br$_2$ (4.4 g, 78% yield).

Synthesis of Tris(4-((trimethylsilyl)ethynyl)phenyl)amine (TPA-TMS). In a solvent mixture comprising 80 mL each of Et$_3$N and THF, 6.00 g of TPA-Br$_3$ was charged (12.42 mmol). Then, 0.206 g of CuI and 0.827 g of PdCl$_2$(PPh$_3$)$_2$ were incorporated into the mixture. The suspension was stirred for 30 min. Subsequently, 12.4 mL of TMS was charged and continued stirring at 80 °C. After 1 day, TPA-TMS was purified via column chromatography, employing *n*-hexane and DCM to confer a light yellow powder [Scheme S3]. FTIR (Figure S7): 3043 and 2157 cm^{-1}. ^1H NMR (Figure S8): 7.34, 6.7, 0.24 ppm. ^{13}C NMR (Figure S9): 147.42−94.42 ppm.

Synthesis of Tris(4-ethynylphenyl)amine (TPA-T). K$_2$CO$_3$ (2.50 g, 18.1 mmol) and TPA-TMS (1.30 g, 2.425 mmol) were agitated in a solvent mixture of MeOH (70 mL) at 25 °C for 2 days. The resultant product subsequently underwent purification, and the solvents were eliminated through column chromatography utilizing a hexane/EA solvent mixture, resulting in the isolation of pure brown powdery TPA-T [Scheme S4]. FTIR (Figure S10): 3266 and 2098 cm^{-1}. ^1H NMR (Figure S11): 7.4, 7.03, and 3.1 ppm. ^{13}C NMR (Figure S12): 148.2−83.6 ppm.

Preparation of TPA-ATQ CMP and TBN-ATQ CMP. ATQ-Br$_2$ (0.5 g) and TBN-T (0.29 g) or TPA-T (0.29 g), CuI (0.01 g), PPh$_3$ (0.02 g), and Pd(PPh$_3$)$_4$ (0.04 g) were inserted into a 50 mL Schlenk flask with a DMF solution (25 mL) and Et$_3$N (25 mL). Then, the flask succumbed to reflux at 90 °C for 72 h. Upon the completion of the reaction, the obtained solid was subjected to Soxhlet extraction in THF and MeOH. Finally, the gathered residue was then dried for 24 h at 100 °C to confer TPA-ATQ CMP as a red solid and TBN-ATQ CMP as a yellow powder.

RESULTS AND DISCUSSION

Synthesis and Characterization of TPA-ATQ CMP and TBN-ATQ CMP. We successfully synthesized pure TPA-ATQ CMP and TBN-ATQ CMP through a Sonogashira coupling reaction, combining TPA-T and TBN-T with brominated ATQ monomers. This method yielded two CMP insoluble solids—red and yellow—with respective yields of 78 and 70%, as detailed in Scheme 1a,b. The synthesis of TPA-T involved the reaction of TPA-TMSA with K$_2$CO$_3$ in a methanol solution. The TBN-T monomer was synthesized by using a three-stage procedure. Initially, TPE-Br$_4$ was reacted with DCM/CH$_3$NO$_2$ and a small amount of anhydrous FeCl$_3$ to yield TBN-Br$_4$.[64] Subsequently, TBN-Br$_4$ was treated with TMSA for 48 h at 25 °C in the presence of PdCl$_2$(PPh$_3$)$_2$, CuI, PPh$_3$, and diethylamine, replacing four C−Br bonds with carbon−carbon triple bonds to form TBN-TMS. Finally, TBN-TMS was hydrolyzed in a methanol solution with K$_2$CO$_3$, converting it to TBN-T. The spectroscopic methods,

https://doi.org/10.1021/acsaem.4c01276
ACS Appl. Energy Mater. 2024, 7, 5582−5593

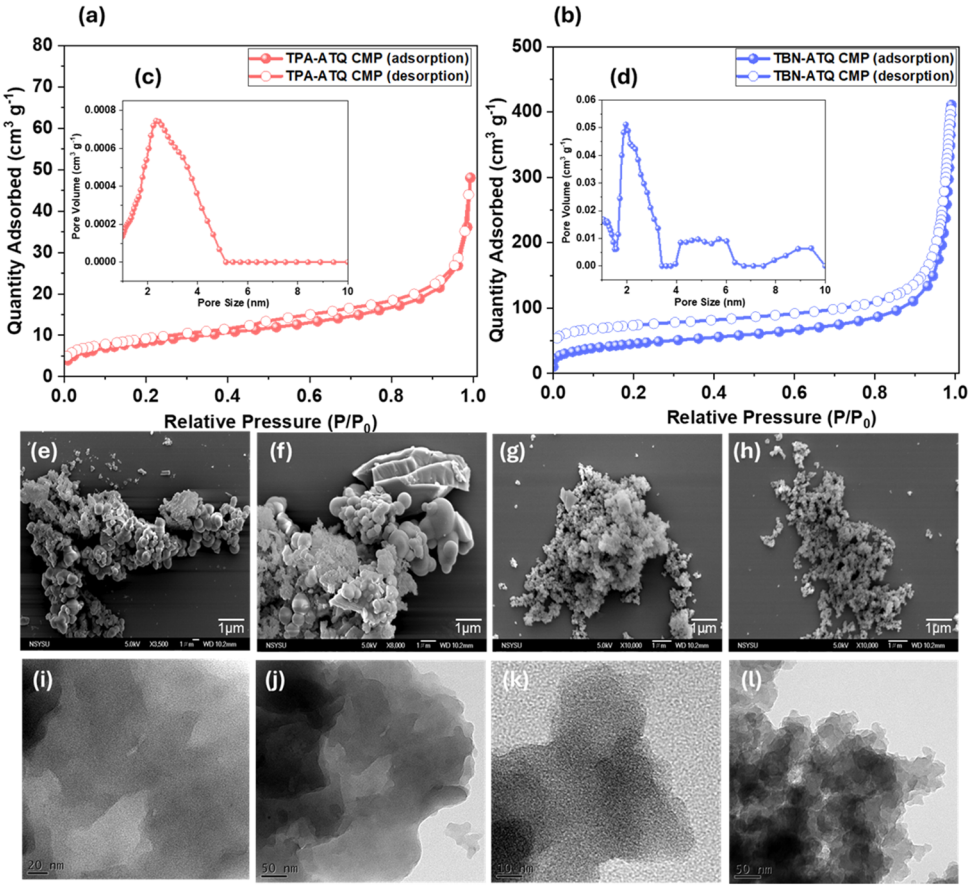

Figure 2. (a, b) N_2 adsorption−desorption, (c, d) pore size profiles, (e−h) SEM, and (i−l) TEM images of (a, c, e, f, i, j) TPA-ATQ CMP and (b, d, g, h, k, l) TBN-ATQ CMP.

specifically FTIR and NMR, employed in the Experimental Section and Supporting Information, verified the successful synthesis of all of the monomers [ATQ-Br_2, TPA-T, and TBN-T] in this study. To analyze the structures of both CMPs (Figure 1), we utilized FTIR and solid-state ^{13}C NMR spectroscopy. The FTIR spectra for ATQ-CMPs [Figure 1a] exhibited absorption peaks at approximately 2205 cm^{-1} (C≡C−H), confirming the presence of alkyne groups within their framework structures. For TPA-ATQ and TBN-ATQ CMPs, aromatic ring vibrations were distinctly observed between 3074 and 3021 cm^{-1}, while the band of C═O appeared at 1763 cm^{-1} (Figure 1a). The solid-state ^{13}C NMR spectrum of TPA-ATQ CMP (Figure 1b) revealed signals at 180.93, 140.31−111.49, and 82.32 ppm. Notably, the peak at 146.77 ppm was attributed to the C−N bond. In the case of TBN-ATQ CMP, carbon nuclei signals were recorded at 180.08, 142.31−113.67, and 81.33 ppm, corresponding to C═O in the ATQ, C═C, and C≡C units, respectively [Figure 1b]. We expanded our investigation of the chemical states of elements within both TPA-ATQ and TBN-ATQ CMPs using X-ray photoelectron spectroscopy (XPS) analysis, as depicted in Figure 1c. Analysis revealed that in the TPA-ATQ CMP framework, carbon (C) was detected at 284.13 eV, nitrogen (N) at 399.32 eV, and oxygen (O) at 531.46 eV. Conversely, in the TBN-ATQ CMP framework, carbon was found at 283.31 eV and oxygen at 532.28 eV. A detailed investigation using solid-state ^{13}C NMR, FTIR, and XPS spectra validated the effective synthesis of the ATQ redox units and their integration as important components in these ATQ-CMPs. TGA conducted in a nitrogen (N_2) environment was used to evaluate the thermal stability of ATQ-CMPs [Figure 1d]. The TPA-ATQ CMP displayed initial thermal degradation temperatures of 321 °C (T_{d5}) and 375 °C (T_{d10}), indicating the temperatures at which 5 and 10% weight loss occurred, respectively. In contrast, the TBN-ATQ CMP demonstrated higher thermal degradation temperatures of 465 (T_{d5}) and 605 °C (T_{d10}). Additionally, the char yields were 64 wt % for TPA-ATQ CMP and 77 wt % for TBN-ATQ CMP, respectively, as illustrated in Figure 1d. These results highlight the superior thermal stability of TBN-ATQ CMP compared to TPA-ATQ CMP.

As shown in Figure 2, Brunauer−Emmett−Teller (BET) analysis demonstrates that the N_2 adsorption−desorption isotherm for the TPA-ATQ CMP aligns with type-III isotherm [Figure 2a], while the TBN-ATQ CMP is classified as type-I isotherm according to IUPAC standards [Figure 2b]. The specific surface area (S_{BET}) for the TPA-ATQ CMP is measured at 35 $m^2\ g^{-1}$, whereas the TBN-ATQ CMP exhibits a significantly larger S_{BET} of 161 $m^2\ g^{-1}$.

Additionally, we employed nonlocal density functional theory to analyze the N_2 sorption isotherms and to model the pore size distributions (PSDs) of both ATQ-CMPs. The analysis revealed that TPA-ATQ and TBN-ATQ CMPs contain primarily micropores, with PSD curves indicating pore sizes of 2.39 nm [Figure 2c] and 1.95−5.13 nm [Figure 2d], respectively. We conducted further investigations into the microstructures of the porous TPA-ATQ and TBN-ATQ CMP using field emission scanning electron microscopy (FE-SEM) and high-resolution transmission electron microscopy (HR-

https://doi.org/10.1021/acsaem.4c01276
ACS Appl. Energy Mater. 2024, 7, 5582−5593

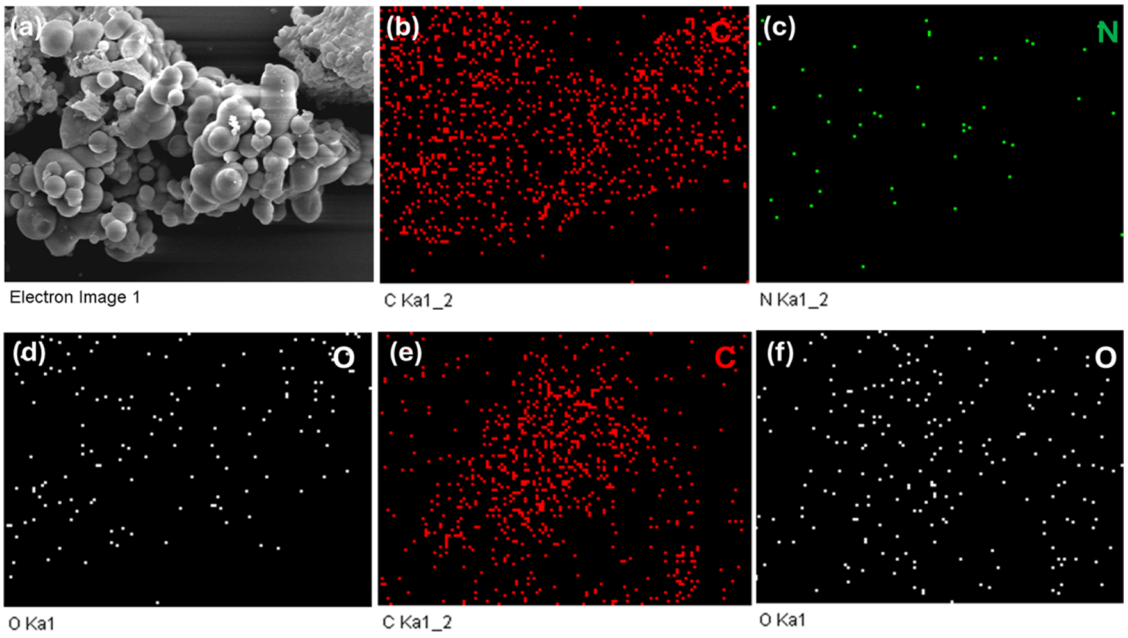

Figure 3. (a–f) SEM-EDS mapping of (a–d) TPA-ATQ CMP and (e, f) TBN-ATQ CMP.

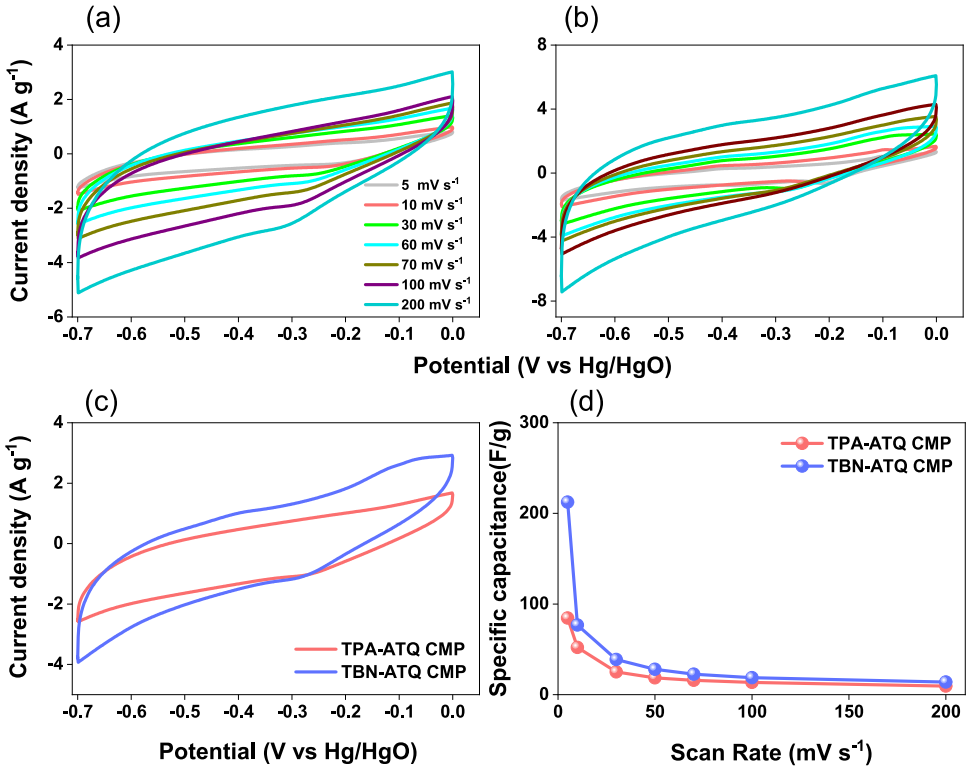

Figure 4. (a) CV curves of TPA-ATQ CMP and (b) TBN-ATQ CMP, (c) CV curves for all of the prepared electrodes at 60 mV s^{-1}, and (d) relation between specific capacitance and its corresponding scan rate for all of the prepared electrodes.

TEM). FE-SEM imaging revealed that both TPA-ATQ CMP and TBN-ATQ CMP displayed spherical shapes with small clusters of spherical particles visible in Figure 2e–h. HR-TEM allowed for detailed observation of the intricate structures characterized by tiny pores, which are visible due to variations in intensity, giving the materials a seemingly uneven and disorganized appearance [Figure 2i–l]. Energy-dispersive X-ray spectroscopy (EDS) images confirmed the presence of carbon (C), nitrogen (N), and oxygen (O) in the materials. Specifically, the TPA-ATQ CMP material consisted of C and O, while the TBN-ATQ CMP material contained C and N [Figure 3a–f].

Electrochemical Performance of TPA-ATQ CMP and TBN-ATQ CMP Based on a Three-Electrode System. Focusing on materials for sustainable energy storage as supercapacitor electrode materials, we have examined TPA-ATQ CMP and TBN-ATQ CMP. We compared the cyclic voltammetry (CV) curves of these materials, generated in a

https://doi.org/10.1021/acsaem.4c01276
ACS Appl. Energy Mater. 2024, 7, 5582–5593

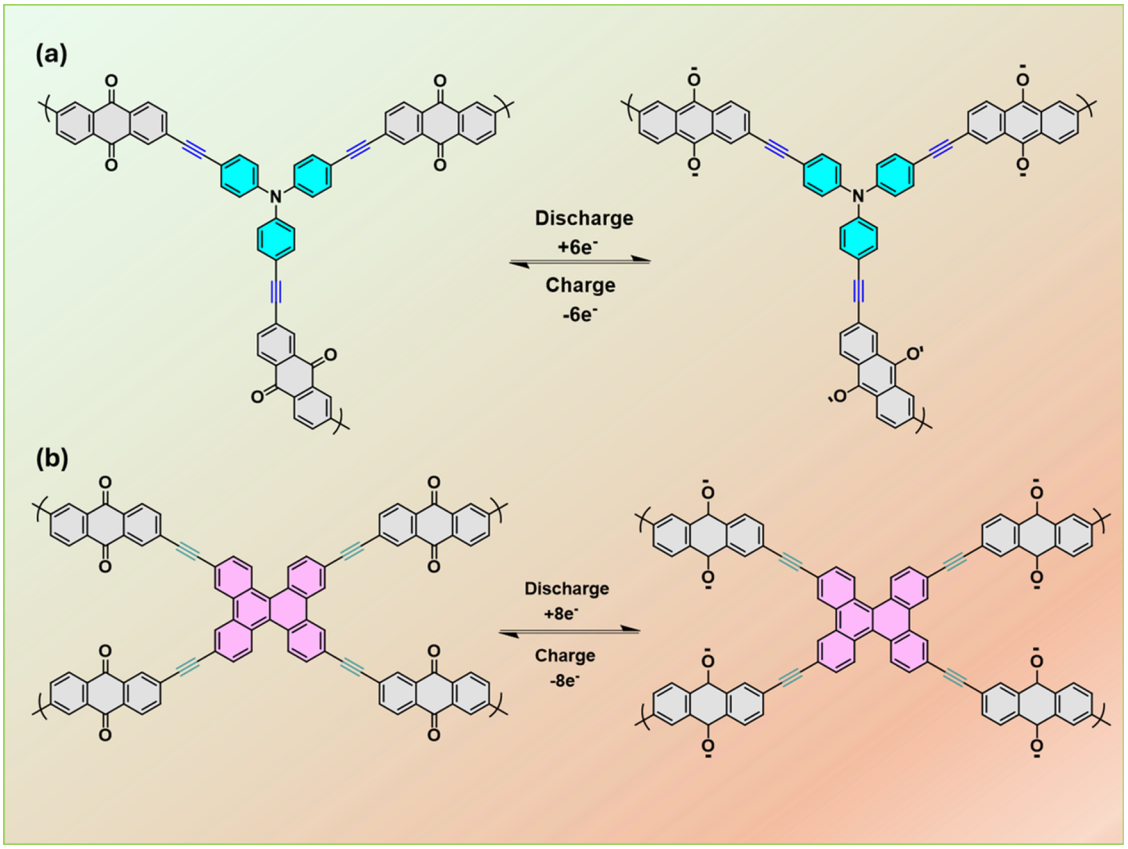

Figure 5. Proposed accessible ATQ redox-active units in (a) TPA-ATQ and (b) TBN-ATQ CMPs during the charge−discharge process.

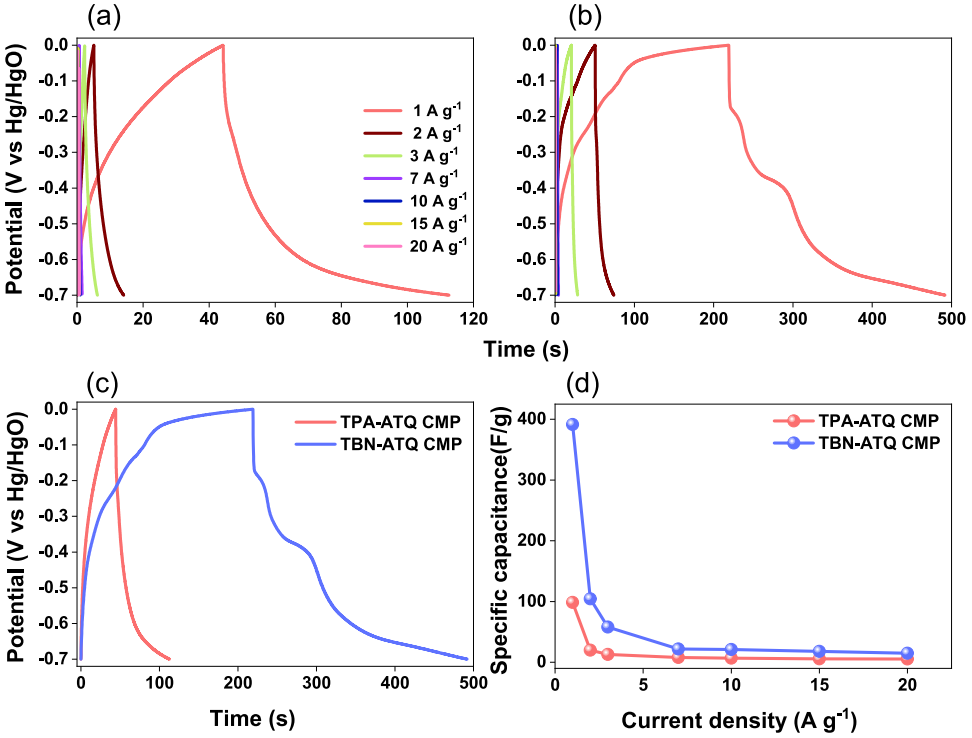

Figure 6. (a) GCD curves of TPA-ATQ and (b) TBN-ATQ CMPs at different current densities. (c) GCD curves for all of the prepared electrodes at 1 A g^{-1} and (d) the relation between specific capacitance and its corresponding current density for all of the prepared electrodes.

three-electrode system using a 1 M KOH electrolyte within a potential window of −0.7 to 0 V. The CV curves of our materials' electrodes displayed rectangular shapes with distinctive humps within this potential range (Figure 4a,b). As the scanning rate increased, the peak current of the TBN-ATQ CMP electrode also increased, indicating low charge

https://doi.org/10.1021/acsaem.4c01276
ACS Appl. Energy Mater. 2024, 7, 5582−5593

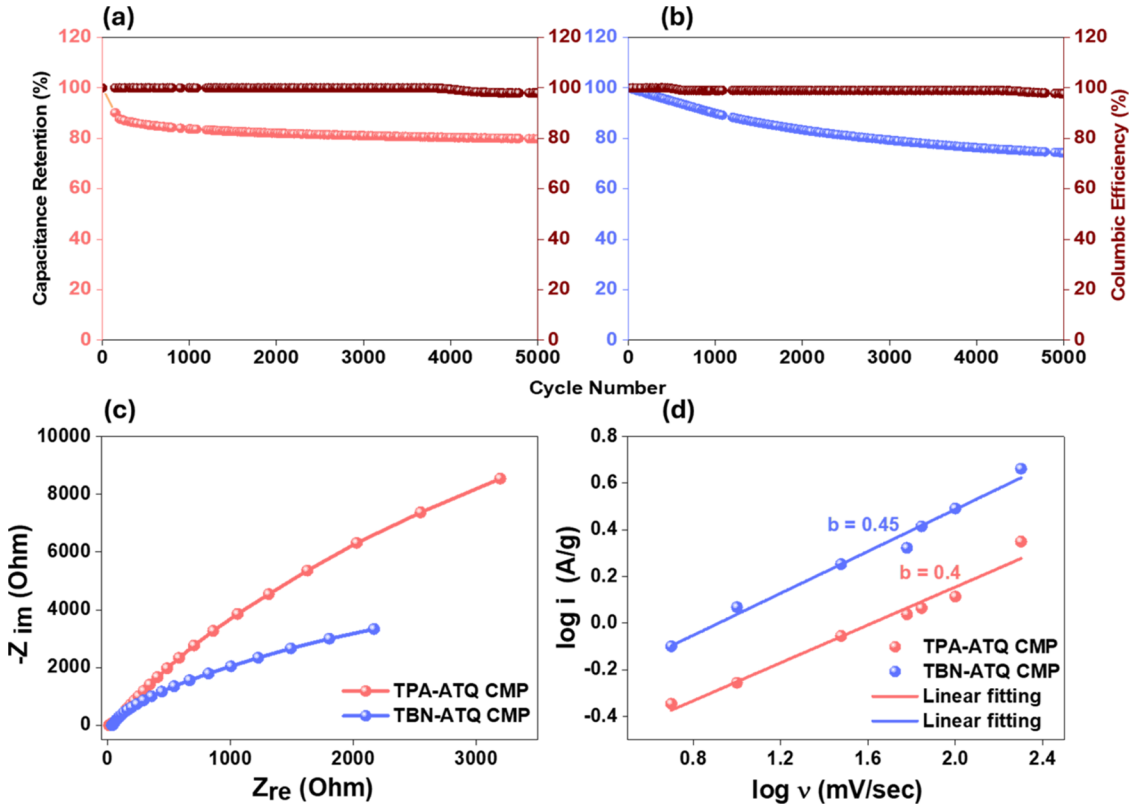

Figure 7. (a, b) Stability test, (c) EIS spectra, and (d) power's law relation for TPA-ATQ CMP and TBN-ATQ CMP electrodes.

transfer resistance and contributions from both pseudocapacitance and electric double-layer capacitance (EDLC) to their capacitive responses.[66] The characteristic humps in the rectangular shapes are attributed to the presence of heteroatoms and electron-rich phenyl rings, enhancing the pseudocapacitance. At a scan rate of 60 mV s^{-1} within the same potential window (−0.7 to 0 V), as illustrated in Figure 4c, the CV curve of TBN-ATQ CMP showed superior charge storage capability with a larger integral area compared to TPA-ATQ CMP. Consequently, as depicted in Figure 4d, TBN-ATQ CMP exhibited higher specific capacitance than TPA-ATQ CMP at various scan rates, with values recorded at 212.5, 76, 38, 28, 22.6, 18.7, and 13.8 C g^{-1} at 5, 10, 30, 60, 70, 100, and 200 mV s^{-1}, respectively. The reversible transformation between quinine and hydroquinone, as depicted in Figure 5a,b, highlights the redox (charge/discharge) process in TPA-ATQ CMP and TBN-ATQ CMP.

This cyclic change underscores their capability for energy storage. For both TPA-ATQ CMP and TBN-ATQ CMP, galvanostatic charge−discharge (GCD) measurements were carried out at 1 to 20 A g^{-1}, as illustrated in Figure 6a,b. The GCD profiles showed a typical triangular shape with slight deviations, reflecting characteristics of both EDLC and pseudocapacitance, consistent with the results observed in the CV analysis. Additionally, the pronounced drop in potential observed at the beginning of each discharge curve in GCD profiles [Figure 6a,b] can be attributed to the internal resistance of the electrode material.[13] Specific GCD measurements at 1 A g^{-1} showed an extended charge−discharge duration for the TBN-ATQ CMP, indicating a higher specific capacitance [Figure 6c]. At this current density, the specific capacitances for TPA-ATQ CMP and TBN-ATQ CMP were calculated based on discharge times to be 99 and 393 F g^{-1}, respectively. Further analysis from the GCD curves (Figure 6d) revealed specific capacitances for TBN-ATQ CMP of 393, 104.2, 57.8, 22, 21, 18, and 15 F g^{-1} at current densities of 1, 2, 3, 7, 10, 15, and 20 A g^{-1}, aligning with the findings from the CV assessments. The higher specific capacitance of TBN-ATQ CMP, nearly 4 times that of TPA-ATQ CMP, is attributed to the slower diffusion rate of electrolyte ions into the material's deeper pores and their limited access to the electrode's surface at increased current densities. Consequently, as the current density increases, ion movement decreases markedly, significantly reducing the specific capacitance. Additionally, Figure S13 and Table S1 offer a comparative analysis of the supercapacitor efficiency between the TBN-ATQ CMP precursor and other CMP materials previously described in the literature. Mei and Li synthesized the CoPc-CMP. By evaluating the GCD curve at 0.5 A/g, the specific capacitance for CoPc-CMP was determined to be 13.8 F g^{-1} in H_2SO_4 (1 M).[67] Similarly, the capacitance of 70.0 F g^{-1} was reported for CuTAPP-CMP/CNTs-1 by the same research group.[68] For the TBN-Py and TBN-Car-CMPs, specific capacitances of 31 and 18.9 F g^{-1} were recorded and analyzed through a GCD curve at 0.5 A g^{-1}.[69] However, the TBN-ATQ CMP outperformed other electrodes in terms of efficiency. Its synthesis method is also cost-effective, straightforward, and scalable for further research.

The cycle stability test is essential for evaluating electrodes' Coulombic efficiency and capacitive retention. Figure 7a,b displays the cycling stability of the TPA-ATQ and TBN-ATQ CMP electrodes, maintaining 79.8 and 74.2% of their original capacitance, respectively, with a Coulombic efficiency of 100% after 5000 charge−discharge cycles. As depicted in Figure 7c, further analysis of the electrodes' electrochemical properties is necessary. The Nyquist plot illustrates the impedance

https://doi.org/10.1021/acsaem.4c01276
ACS Appl. Energy Mater. 2024, 7, 5582−5593

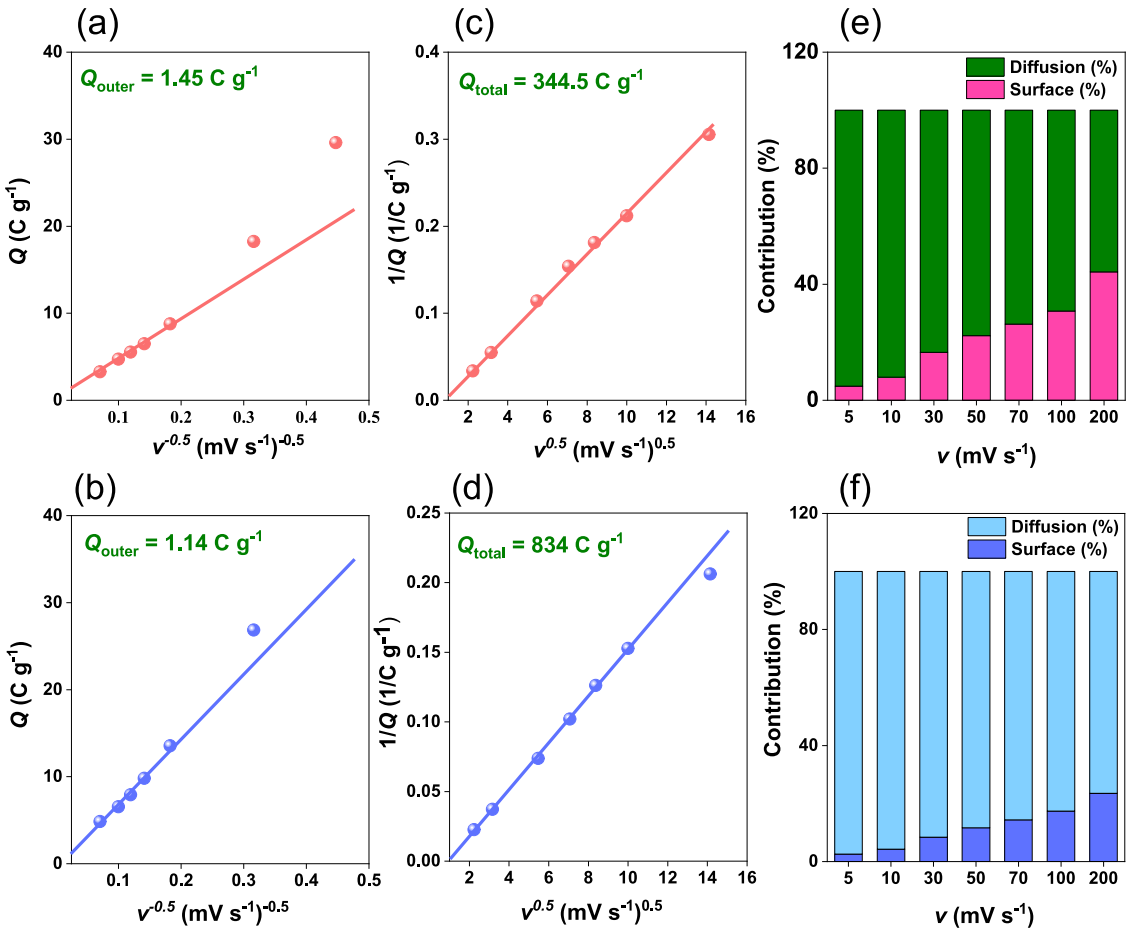

Figure 8. (a, b) Relation between Q (C g^{-1}) and $v^{-0.5}$ (mV s^{-1})$^{-0.5}$, (c, d) $1/Q$ vs $v^{0.5}$ (mV s^{-1})$^{0.5}$, and (e, f) percentage of surface contribution and diffusion contribution for (a, c, e) TPA-ATQ CMP and (b, d, f) TBN-ATQ CMP electrodes.

spectrum, ranging from 100 kHz to 100 MHz, which shows a semicircular shape at high frequencies and a straight line in the low-frequency region. The initial intersection of the Nyquist plot with the real axis (X-axis) represents the solution resistance, encompassing the intrinsic resistance of the electrodes, the ionic resistance of the KOH electrolyte, the internal resistance within the electrode material, and the interfacial resistance between the electrode surface and the electrolyte solution. The charge transfer resistance, reflected by the semicircle's diameter in the high-frequency region, is minimized to enhance the electrodes' access to the electrolyte solution. The slope in the low-frequency part of the Nyquist plot, indicative of diffusive resistance, relates to Warburg impedance, which characterizes the diffusion of electrolyte ions and electrons through the electrode, demonstrating their ease of movement. CV is considered the most critical technique for analyzing a material's electrochemical behavior across a voltage range, providing insights into its operational voltage, reversibility, kinetics (diffusion versus surface control), and energy storage mechanisms. Following electrochemical analysis, the capacitive contribution to total charge storage was further explored. The power law, represented by the equation $i(V) = av^b$ or ($\log i = a + b \log \nu$), where ν is the applied potential window and i is the applied current density, was utilized to study the charge storage capabilities of the electrodes, as shown in Figure 7d. The intercept and the slope of the log i versus log v plots help determine the constant parameters a and b. As indicated in Figure 7d, the calculated b-values for TPA-ATQ and TBN-ATQ CMPs are 0.4 and 0.45, respectively, approximating 0.5. This suggests that the charge storage mechanism predominantly operates under diffusion control. Additionally, Figure 8a–f illustrates the distribution of capacitive and diffusive current-controlled contributions for the electrodes of the TPA-ATQ and TBN-ATQ CMPs. To properly execute the charging harvesting mechanism, the percentages of diffusion-controlled and surface-controlled capacitive processes to the total charge obtained (Q total) must be calculated. Only surface operations occurred when the applied potential sweep rate reached its maximum value, and the stored charge in this instance is the outer charge (Q outer) according to the Trasatti effort. The relationship between capacity Q and $(\nu)^{-0.5}$, where (ν) is the potential scan rate, is depicted in Figure 8a,b. The value of (Q outer) can be determined in line with the relationship by calculating the intercept of the relationship between Q and $(\nu)^{-0.5}$

$$Q = Q_{outer} + K\nu^{-0.5}$$

where ν (mV s^{-1}) represents the potential scan rate, K is the constant, and Q (C g^{-1}) specifies the capacity generated from each CV pattern. However, in this case, the stored charge occurs when the potential scan rate reaches its minimal values, which provides enough time for the ions to diffuse. This is known as the total charge (Q total), which can be obtained by

https://doi.org/10.1021/acsaem.4c01276
ACS Appl. Energy Mater. 2024, 7, 5582−5593

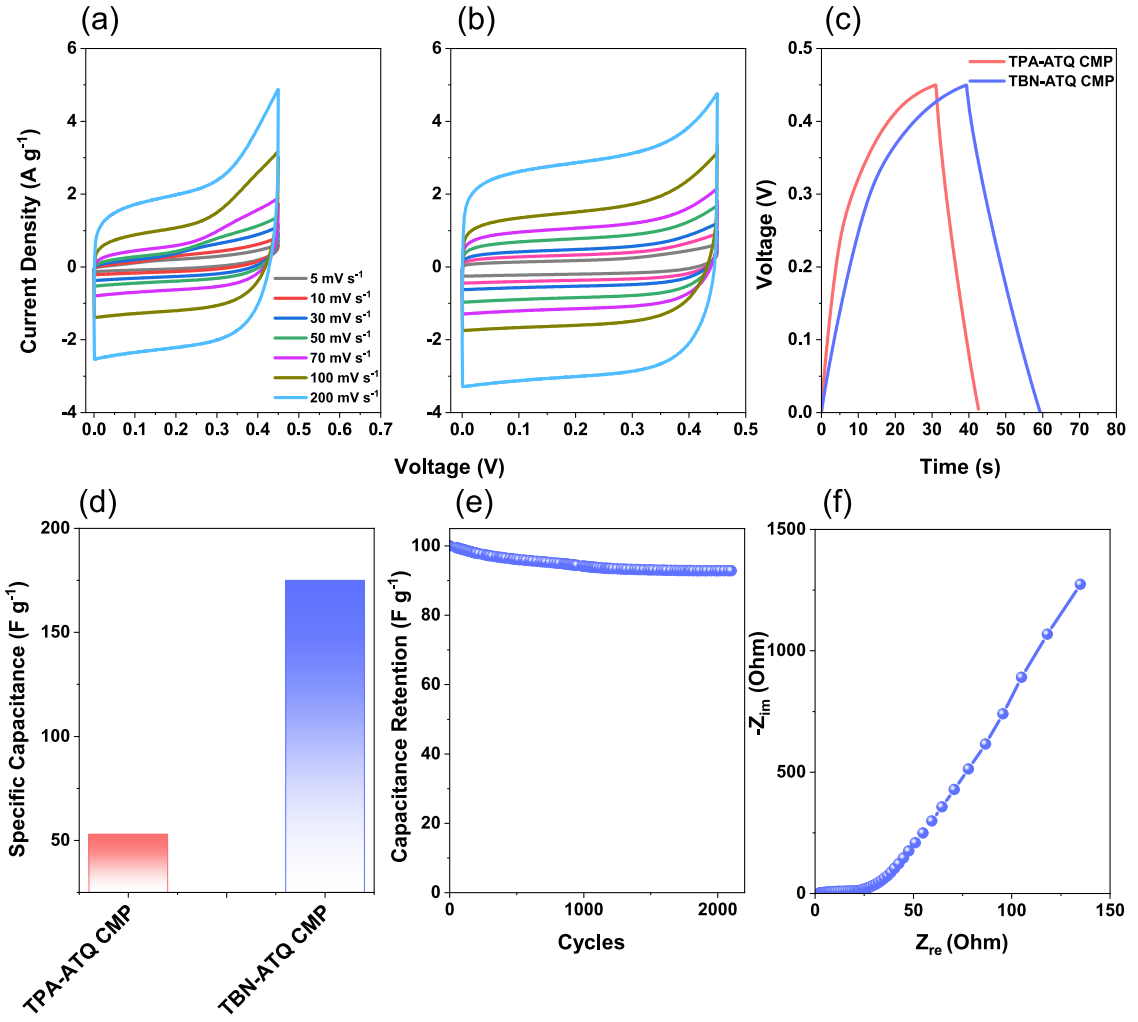

Figure 9. (a) CV curves of TPA-ATQ CMP and (b) TBN-ATQ CMP, (c) GCD curves of ATQ-CMPs at 1 A g^{-1}, (d) calculated specific capacitance of TPA-ATQ and TBN-ATQ CMP at 1 A g^{-1}, (e) stability test, and (f) EIS spectrum of TBN-ATQ CMP (based on symmetric coin cell measurements).

plotting $1/Q$ against $(v)^{0.5}$, as shown in Figure 8c,d. According to the partnership

$$\frac{1}{Q} = \frac{1}{Q_{\text{total}}} + Kv^{0.5}$$

Thus, Figure 8e,f shows the surface- and diffusion-controlled contribution percentage at scan rates. The yields of diffusion-controlled faradic TPA-ATQ CMP and TBN-ATQ CMP are 95.1 and 97.4%, respectively. Significant diffusion-controlled contributions were observed for all electrodes at all scan rates, which is consistent with the electrodes acting like batteries during the charge/discharge cycle.

We evaluated the electrochemical performance of TPA-ATQ and TBN-ATQ CMPs for long-term applications by assembling them into symmetric coin cells. The results from a series of CV tests on these devices are depicted in Figure 9a,b. We expanded the operational voltage window of the device from 0 to 0.45 V. The CV curves remained rectangular, indicating the combined influence of pseudocapacitive behavior and EDLC relative to the electrode materials. We performed GCD analyses of ATQ-CMPs at 1 A g^{-1}, as shown in Figure 9c, and the nonlinear charge/discharge plateaus demonstrate the pseudocapacitance and EDLC characteristics of the symmetric coin cell. We also calculated the specific capacitance values for each device using the GCD curves; TPA-ATQ and TBN-ATQ CMP values were 53 and 175 F g^{-1}, respectively [Figure 9d]. The symmetric coin cell device of TBN-ATQ CMP retained 92.8% of its initial capacity after 2000 consecutive charge/discharge cycles at 10 A g^{-1}, indicating robust durability and performance, as well as reversible functionality, as shown in Figure 9e. Figure 9f illustrates the EIS of the symmetric TBN-ATQ CMP device. In the high-frequency range, a tiny semicircle is displayed that symbolizes the fundamental resistive characteristics of the supercapacitor system, which includes the electrode, electrolyte, and current collector. The semicircle originates at the intersection of the Z' axis and Z'' axis from the left, symbolizing the electrolyte's resistance (R_s) in contact with the electrode and current collector. The end point is located at the precise intersection of Z'' and the Z' axis, indicating the electrode's internal resistance (R_p). Subtracting R_s from R_p yields the value of the equivalent series resistance (ESR), which determines the width of the semicircle. In the low-frequency domain, the presence of steeply ascending straight lines indicates capacitive dominance caused by the generation of electronic and ionic charges on the surfaces within the micropores of the electric double-layer system. Notably, the

https://doi.org/10.1021/acsaem.4c01276
ACS Appl. Energy Mater. 2024, 7, 5582−5593

vertical line on the cell's axis suggests a higher Warburg length or resistance. Overall, these findings underscore the potential of the TBN-ATQ CMP for supercapacitor (SC) applications and validate a viable synthesis approach.

CONCLUSIONS

In summary, the Sonogashira coupling method facilitated the production of ATQ-based CMPs (ATQ-CMPs), namely, TPA-ATQ CMP and TBN-ATQ CMP. These materials exhibit characteristics that are highly beneficial for energy storage, particularly in supercapacitor (SC) applications. Both ATQ-CMPs demonstrated impressive thermal stability with high T_{d10} values of 465 °C for TPA-ATQ CMP and 605 °C for TBN-ATQ CMP. In terms of electrochemical properties, TBN-ATQ CMP surpassed the other TPA-ATQ-CMP, showcasing a high specific capacitance of 393 F g^{-1} and excellent capacity retention across numerous cycles. The superior performance of the TBN-ATQ CMP is likely attributed to its larger S_{BET} (161 m^2 g^{-1}), greater total pore volume (0.63 cm^3 g^{-1}), and presence of phenyl rings. The unique surface characteristics and chemical structure of the TBN-ATQ CMP electrode, which enhances its conductivity, highlight the potential of CMPs as very effective materials for enhancing energy storage technology.

ASSOCIATED CONTENT

Supporting Information

The Supporting Information is available free of charge at https://pubs.acs.org/doi/10.1021/acsaem.4c01276.

Characterization methods and electrochemical analysis, as well as the synthesis of TBN-TMS and TBN-T monomers; FTIR, ^{1}H NMR, and ^{13}C NMR data of the synthesized monomers; comparison of the specific capacitance of TPA-ATQ CMP and TBN-ATQ CMP with those of previously reported materials for supercapacitor application (PDF)

AUTHOR INFORMATION

Corresponding Authors

Mohamed Gamal Mohamed − *Department of Materials and Optoelectronic Science, College of Semiconductor and Advanced Technology Research, Center for Functional Polymers and Supramolecular Materials, National Sun Yat-Sen University, Kaohsiung 804, Taiwan; Department of Chemistry, Faculty of Science, Assiut University, Assiut 71516, Egypt;* orcid.org/0000-0003-0301-8372; Email: mgamal.eldin12@yahoo.com

Shiao-Wei Kuo − *Department of Materials and Optoelectronic Science, College of Semiconductor and Advanced Technology Research, Center for Functional Polymers and Supramolecular Materials, National Sun Yat-Sen University, Kaohsiung 804, Taiwan; Department of Medicinal and Applied Chemistry, Kaohsiung Medical University, Kaohsiung 807, Taiwan;* orcid.org/0000-0002-4306-7171; Email: kuosw@faculty.nsysu.edu.tw

Authors

Mervat Ibrahim − *Chemistry Department, Faculty of Science, New Valley University, El-Kharja 72511, Egypt*

Nian Ping Chen − *Department of Materials and Optoelectronic Science, College of Semiconductor and Advanced Technology Research, Center for Functional Polymers and Supramolecular Materials, National Sun Yat-Sen University, Kaohsiung 804, Taiwan*

Abdul Basit − *Department of Materials and Optoelectronic Science, College of Semiconductor and Advanced Technology Research, Center for Functional Polymers and Supramolecular Materials, National Sun Yat-Sen University, Kaohsiung 804, Taiwan*

Yang Chin Kao − *Department of Materials and Optoelectronic Science, College of Semiconductor and Advanced Technology Research, Center for Functional Polymers and Supramolecular Materials, National Sun Yat-Sen University, Kaohsiung 804, Taiwan*

Aya Osama Mousa − *Department of Materials and Optoelectronic Science, College of Semiconductor and Advanced Technology Research, Center for Functional Polymers and Supramolecular Materials, National Sun Yat-Sen University, Kaohsiung 804, Taiwan*

Maha Mohamed Samy − *Department of Materials and Optoelectronic Science, College of Semiconductor and Advanced Technology Research, Center for Functional Polymers and Supramolecular Materials, National Sun Yat-Sen University, Kaohsiung 804, Taiwan; Department of Chemistry, Faculty of Science, Assiut University, Assiut 71516, Egypt*

Complete contact information is available at: https://pubs.acs.org/10.1021/acsaem.4c01276

Author Contributions

$^{\perp}$M.G.M. and M.I. contributed equally to this work.

Notes

The authors declare no competing financial interest.

ACKNOWLEDGMENTS

This study was supported financially by the National Science and Technology Council, Taiwan, under contracts NSTC 112−2223-E-110-002- and 112-2218-E-110-007. The authors thank the staff at the National Sun Yat-sen University for their assistance with the TEM (ID: EM022600) experiments.

REFERENCES

(1) Libich, J.; Máca, J.; Vondrák, J.; Čech, O.; Sedlaříková, M. Supercapacitors: Properties and applications. *J. Energy Storage* **2018**, *17*, 224−227.

(2) Mousa, A. O.; Sharma, S. U.; Chaganti, S. V.; Mansoure, T. H.; Singh, P. N.; Ejaz, M.; Chuang, C. H.; Lee, J. T.; Kuo, S. W.; Mohamed, M. G. Designing strategically functionalized conjugated microporous polymers with pyrene and perylenetetracarboxylic dianhydride moieties with single-walled carbon nanotubes to enhance supercapacitive energy storage efficiency. *J. Power Sources* **2024**, *608*, No. 234624.

(3) Mohamed, M. G.; Elsayed, M. H.; Hassan, A. E.; Basit, A.; Mekhemer, I. M. A.; Chou, H. H.; Chen, K. H.; Kuo, S. W. Hybrid Porous Polymers Combination of Octavinylsilsesquioxane/Pyrene with Benzothiadiazole Units for Robust Energy Storage and Efficient Photocatalytic Hydrogen Production from Water. *ACS Appl. Polym. Mater.* **2024**, *6*, 5945−5956.

(4) Wang, S. H.; Li, L.; Wang, H.; Wang, X. W.; Wang, T. H. Continuous and Scalable Manufacture of Coal-Derived Hierarchical Porous Carbon Dominated with Mesopores for High Rate-Performance Supercapacitors. *ACS Appl. Energy Mater.* **2024**, *7*, 4268−4278.

(5) Mohamed, M. G.; Ahmed, M. M.; Du, W. T.; Kuo, S. W. Meso/Microporous Carbons from Conjugated Hyper-Crosslinked Polymers Based on Tetraphenylethene for High-Performance CO_2 Capture and Supercapacitor. *Molecules* **2021**, *26*, No. 738.

(6) Yu, Z.; Tetard, L.; Zhai, L.; Thomas, J. Supercapacitor electrode materials: Nanostructures from 0 to 3 dimensions. *Energy Environ. Sci.* **2015**, *8*, 702−730.
(7) Weng, T. H.; Mohamed, M. G.; Sharma, S. U.; Mekhemer, I. M. A.; Chou, H. H.; Kuo, S. W. Rationally Engineered Ultrastable Three-Dimensional (3D) Conjugated Microporous Polymers Containing Triptycene, Tetraphenylethene, and Benzothiadiazole Units as Exceptional High-Performance Organic Electrodes for Supercapacitors. *ACS Appl. Energy Mater.* **2023**, *6*, 9012−902457.
(8) Singh, P. N.; Mohamed, M. G.; Kuo, S. W. Systematic Design and Synthesis of Conjugated Microporous Polymers Containing Pyrene and Azobenzene Building Materials for High-Performance Energy Storage. *ACS Appl. Energy Mater.* **2023**, *6*, 11342−11351.
(9) Libich, J.; Máca, J.; Vondrák, J.; Čech, O.; Sedlaříková, M. Supercapacitors: Properties and applications. *J. Energy Storage* **2018**, *17*, 224−227.
(10) Mohamed, M. G.; Sharma, S. U.; Liu, N. Y.; Mansoure, T. H.; Samy, M. M.; Chaganti, S. V.; Chang, Y. L.; Lee, J. T.; Kuo, S. W. Ultrastable covalent triazine organic framework based on anthracene moiety as a platform for high-performance carbon dioxide adsorption and supercapacitors. *Int. J. Mol. Sci.* **2022**, *23*, No. 3174.
(11) Mohamed, M. G.; Chaganti, S. V.; Li, M. S.; Samy, M. M.; Sharma, S. U.; Lee, J. T.; Elsayed, M. H.; Chou, H. H.; Kuo, S. W. Ultrastable Porous Organic Polymers Containing Thianthrene and Pyrene Units as Organic Electrode Materials for Supercapacitors. *ACS Appl. Energy Mater.* **2022**, *5*, 6442−6452.
(12) Mohamed, M. G.; Mohamed, H. E.; Ahmed, E. H.; Abdul, B.; Islam, M. A. M.; Chou, H. H.; Chen, K. H.; Kuo, S. W. Hybrid Porous Polymers Combination of Octavinylsilsesquioxane/Pyrene with Benzothiadiazole Units for Robust Energy Storage and Efficient Photocatalytic Hydrogen Production from Water. *ACS Appl. Polym. Mater.* **2024**, *6*, 5945−5956.
(13) Zhao, X.; Sajjad, M.; Zheng, Y.; Zhao, M.; Li, Z.; Wu, Z.; Kang, K.; Qiu, L. Covalent organic framework templated ordered nanoporous C_{60} as stable energy efficient supercapacitor electrode material. *Carbon* **2021**, *182*, 144−154.
(14) Samy, M. M.; Mohamed, M. G.; Sharma, S. U.; Chaganti, S. V.; Mansoure, T. H.; Lee, J. T.; Chen, T.; Kuo, S. W. Constructing conjugated microporous polymers containing triphenylamine moieties for high-performance capacitive energy storage. *Polymer* **2023**, *264*, No. 125541.
(15) Samy, M. M.; Mohamed, M. G.; Kuo, S. W. Directly synthesized nitrogen-and-oxygen−doped microporous carbons derived from a bio-derived polybenzoxazine exhibiting high-performance supercapacitance and CO_2 uptake. *Eur. Polym. J.* **2020**, *138*, No. 109954.
(16) Mohamed, M. G.; Samy, M. M.; Mansoure, T. H.; Li, C. J.; Li, W. C.; Chen, J. H.; Zhang, K.; Kuo, S. W. Microporous Carbon, and Carbon/Metal Composite Materials Derived from Bio-Benzoxazine-Linked Precursor for CO_2 Capture and Energy Storage Applications. *Int. J. Mol. Sci.* **2022**, *23*, No. 347.
(17) Mohamed, M. G.; Chaganti, S. V.; Li, M. S.; Samy, M. M.; Sharma, S. U.; Lee, J. T.; Elsayed, M. H.; Chou, H. H.; Kuo, S. W. Ultrastable Porous Organic Polymers Containing Thianthrene and Pyrene Units as Organic Electrode Materials for Supercapacitors. *ACS Appl. Energy Mater.* **2022**, *5*, 6442−6452.
(18) Mousa, A. O.; Mohamed, M. G.; Chuang, C. H.; Kuo, S. W. Carbonized Aminal-Linked Porous Organic Polymers Containing Pyrene and Triazine Units for Gas Uptake and Energy Storage. *Polymers* **2023**, *15*, No. 1891.
(19) Mohamed, M. G.; Hu, H. Y.; Madhu, M.; Samy, M. M.; Mekhemer, I. M. A.; Tseng, W. L.; Chou, H. H.; Kuo, S. W. Ultrastable Two-Dimensional Fluorescent Conjugated Microporous Polymers Containing Pyrene and Fluorene Units for Metal Ion Sensing and Energy Storage. *Eur. Polym. J.* **2023**, *189*, No. 111980.
(20) Samy, M. M.; Mohamed, M. G.; Kuo, S. W. Conjugated Microporous Polymers Based on Ferrocene Units as Highly Efficient Electrodes for Energy Storage. *Polymers* **2023**, *15*, No. 1095.
(21) Mousa, A. O.; Chuang, C. H.; Kuo, S. W.; Mohamed, M. G. Strategic Design and Synthesis of Ferrocene Linked Porous Organic Frameworks toward Tunable CO_2 Capture and Energy Storage. *Int. J. Mol. Sci.* **2023**, *24*, No. 12371.
(22) Mohamed, M. G.; Chang, S. Y.; Ejaz, M.; Samy, M. M.; Mousa, A. O.; Kuo, S. W. Design and Synthesis of Bisulfone-Linked Two-Dimensional Conjugated Microporous Polymers for CO_2 adsorption and Energy Storage. *Molecules* **2023**, *28*, No. 3234.
(23) Zhao, M.; Zhao, Q.; Li, B.; Xue, H.; Pang, H.; Chen, C. Recent progress in layered double hydroxide based materials for electrochemical capacitors: Design, synthesis and performance. *Nanoscale* **2017**, *9*, 15206−15225.
(24) Winter, M.; Brodd, R. J. What are batteries, fuel cells, and supercapacitors? *Chem. Rev.* **2004**, *104*, 4245−4269.
(25) Zhang, L. L.; Zhao, X. S. Carbon-based materials as supercapacitor electrodes. *Chem. Soc. Rev.* **2009**, *38*, 2520−2531.
(26) Ejaz, M.; Mohamed, M. G.; Huang, W. C.; Kuo, S. W. Pyrene-based covalent organic polymers with nano carbonaceous composites for efficient supercapacitive energy storage. *J. Mater. Chem. A* **2023**, *11*, 22868−22883.
(27) Chen, C. Y.; Mohamed, M. G.; Chen, W. C.; Kuo, S. W. Construction of Ultrastable porous carbons materials derived from organic/inorganic double-decker silsesquioxane (DDSQ) hybrid as a high-performance electrode for supercapacitor. *Mater. Today Chem.* **2023**, *34*, No. 101773.
(28) Singh, P. N.; Mohamed, M. G.; Chaganti, S. V.; Sharma, S. U.; Ejaz, M.; Lee, J. T.; Kuo, S. W. Rational Design of Ultrastable Conjugated Microporous Polymers Based on Pyrene and Perylene Units as High-Performance Organic Electrode Materials for Supercapacitor Applications. *ACS Appl. Energy Mater.* **2023**, *6*, 8277−8287.
(29) Samy, M. M.; Mohamed, M. G.; Kuo, S. W. Pyrene-functionalized tetraphenylethylene polybenzoxazine for dispersing single-walled carbon nanotubes and energy storage. *Compos. Sci. Technol.* **2020**, *199*, No. 108360.
(30) Xu, L.; Wang, F.; Ge, X.; Liu, R.; Xu, M.; Yang, J. Covalent organic frameworks on reduced graphene oxide with enhanced electrochemical performance. *Microporous Mesoporous Mater.* **2019**, *287*, 65−70.
(31) Shao, Y.; El-Kady, M. F.; Sun, J.; Li, Y.; Zhang, Q.; Zhu, M.; Wang, H.; Dunn, B.; Kaner, R. B. Design and Mechanisms of Asymmetric Supercapacitors. *Chem. Rev.* **2018**, *118*, 9233−9280.
(32) Ejaz, M.; Mohamed, M. G.; Chen, Y. T.; Zhang, K.; Kuo, S.-W. Porous carbon materials augmented with heteroatoms derived from hyperbranched biobased benzoxazine resins for enhanced CO_2 adsorption and exceptional supercapacitor performance. *J. Energy Storage* **2024**, *78*, No. 110166.
(33) Geioushy, R. A.; Attia, S. Y.; Mohamed, S. G.; A, R. A.; Fouad, O. A. Polyvinylpyrrolidone and freeze drying-assisted growth of an α-$Ni(OH)_2$/reduced graphene oxide hybrid structure as a superior electrode material for supercapacitors. *New J. Chem.* **2021**, *45*, 10012−10020.
(34) Mei, L.; Cui, X.; Duan, Q.; Li, Y.; Lv, X.; Wang, H. Metal phthalocyanine-linked conjugated microporous polymer hybridized with carbon nanotubes as a high-performance flexible electrode for supercapacitors. *Int. J. Hydrogen Energy* **2020**, *45*, 22950−22958.
(35) Bennett, T. D.; Coudert, F. X.; James, S. L.; Cooper, A. I. The changing state of porous materials. *Nat. Mater.* **2021**, *20*, 1179−1187.
(36) Sun, J.; Cao, W.; Pan, S.; He, L.; Ji, D.; Zheng, N.; Sun, X.; Wang, R.; Niu, Y. Porous Organic Materials in Tissue Engineering: Recent Advances and Applications for Severed Facial Nerve Injury Repair. *Molecules* **2024**, *29*, No. 566.
(37) Dong, X. Y.; Zhao, H. X.; Zhang, K. K.; Lang, X. J. Pyrene-based porous organic materials for visible light photocatalysis. *Coord. Chem. Rev.* **2024**, *513*, No. 215902.
(38) Nayak, B.; Mukherjee, A.; Basu, S.; Bhanja, P.; Jena, B. K. Metal-Free Triazine-Based Porous Organic Polymer-Derived N-Doped Porous Carbons as Effective Electrocatalysts for Oxygen Reduction Reaction. *ACS Appl. Energy Mater.* **2022**, *5*, 15899−15908.

https://doi.org/10.1021/acsaem.4c01276
ACS Appl. Energy Mater. 2024, 7, 5582−5593

(39) Liao, B. C.; Jian, B. H.; Wu, M. J.; Lee, J. T. Designing 3D Porous Organic Polymers for High-Performance Organic Battery Cathodes. *ACS Appl. Energy Mater.* **2023**, *6*, 8581−8589.
(40) Lee, J. S. M.; Cooper, A. I. Advances in Conjugated Microporous Polymers. *Chem. Rev.* **2020**, *120*, 2171−2214.
(41) Cooper, A. I. Conjugated Microporous Polymers. *Adv. Mater.* **2009**, *21*, 1291−1295.
(42) Mohamed, M. G.; EL-Mahdy, A. F.; Kotp, M. G.; Kuo, S. W. Advances in porous organic polymers: syntheses, structures, and diverse applications. *Mater. Adv.* **2022**, *3*, 707−733.
(43) Xu, Y.; Jin, S.; Xu, H.; Nagai, A.; Jiang, D. Conjugated Microporous Polymers: Design, Synthesis and Application. *Chem. Soc. Rev.* **2013**, *42*, 8012−8031.
(44) Wang, L.; Wan, Y.; Ding, Y.; Wu, S.; Zhang, Y.; Zhang, X.; Zhang, G.; Xiong, Y.; Wu, X.; Yang, J.; Xu, H. Conjugated Microporous Polymer Nanosheets for Overall Water Splitting Using Visible Light. *Adv. Mater.* **2017**, *29*, No. 1702428.
(45) I Said, A.; Mohamed, M. G.; Madhu, M.; Singh, P. N.; Chaganti, S. V.; Elsayed, M. H.; Tseng, W. L.; Raymo, F. M.; Kuo, S. W. Bifunctional luminescent conjugated microporous polymers containing BODIPY and tetraphenylethene units for highly efficient energy storage and enhanced sensing of Cu^{2+} ions. *Polymer* **2024**, *300*, No. 126988.
(46) Mohamed, M. G.; Atayde, E. C., Jr.; Matsagar, B. M.; Yamauchi, Y.; Wu, K. C.-W.; Kuo, S.-W. Construction Hierarchically Mesoporous/Microporous Materials Based on Block Copolymer and Covalent Organic Framework. *J. Taiwan Inst. Chem. Eng.* **2020**, *112*, 180−192.
(47) Kang, H.; Liu, H.; Li, C.; Sun, L.; Zhang, C.; Gao, H.; Yin, J.; Yang, B.; You, Y.; Jiang, K.-C.; et al. Polyanthraquinone-triazine—A promising anode material for high-energy lithium-ion batteries. *ACS Appl. Mater.* **2018**, *10*, 37023−37030.
(48) Amin, K.; Ashraf, N.; Ma, L.; Faul, C. F. J.; Wei, Z. Conjugated microporous polymers for energy storage: Recent progress and challenges. *Nano Energy* **2021**, *85*, No. 105958.
(49) Chen, J.; Qiu, T.; Yan, W.; Faul, C. F. J. Exploiting Hansen solubility parameters to tune porosity and function in conjugated microporous polymers. *J. Mater. Chem. A* **2020**, *8*, 22657−22665.
(50) Suzuki, A. Cross-Coupling Reactions Of Organoboranes: An Easy Way To Construct C-C Bonds (Nobel Lecture). *Angew. Chem., Int. Ed.* **2011**, *50*, 6722−6737.
(51) Mousa, A. O.; Mohamed, M. G.; Lin, Z. I.; Chuang, C. H.; Chen, C. K.; Kuo, S. W. Construction of cationic conjugated microporous polymers containing pyrene units through post-cationic modification for enhanced antibacterial performance. *J. Taiwan Inst. Chem. Eng.* **2024**, *157*, No. 105448.
(52) Mohamed, M. G.; Elsayed, M. H.; Li, C. J.; Hassan, A. E.; Mekhemer, I. M. A.; Musa, A. F.; Hussien, M. K.; Chen, L. C.; Chen, K. H.; Chou, H. H.; Kuo, S. W. Reticular design and alkyne bridge engineering in donor−π−acceptor type conjugated microporous polymers for boosting photocatalytic hydrogen evolution. *J. Mater. Chem. A* **2024**, *12*, 7693−7710.
(53) Sharma, S. U.; Elsayed, M. H.; Mekhemer, I. M. A.; Meng, T. S.; Chou, H. H.; Kuo, S. W.; Mohamed, M. G. Rational design of pyrene and thienyltriazine-based conjugated microporous polymers for high-performance energy storage and visible-light photocatalytic hydrogen evolution from water. *Giant* **2024**, *17*, No. 100217.
(54) Luo, S.; Zeng, Z.; Wang, H.; Xiong, W.; Song, B.; Zhou, C.; Duan, A.; Tan, X.; He, Q.; Zeng, G.; Liu, Z.; Xiao, R. Recent progress in conjugated microporous polymers for clean energy: Synthesis, modification, computer simulations, and applications. *Prog. Polym. Sci.* **2021**, *115*, No. 101374.
(55) Hayat, A.; Sohail, M.; El-Jery, A.; Al-Zaydi, K. M.; Raza, S.; Ali, H.; Al-Hadeethi, Y.; Taha, T. A.; Din, I. U.; Khan, M. A.; Amin, M. A.; Ghasali, E.; Orooji, Y.; Ajmal, Z.; Ansari, M. Z. Recent advances in ground-breaking conjugated microporous polymers-based materials, their synthesis, modification and potential applications. *Mater. Today* **2023**, *64*, 180−208.
(56) Luo, S.; Zeng, Z.; Zeng, G.; Liu, Z.; Xiao, R.; Xu, P.; Wang, H.; Huang, D.; Liu, Y.; Shao, B.; Liang, Q.; Wang, D.; He, Q.; Qin, L.; Fu, Y. Recent advances in conjugated microporous polymers for photocatalysis: designs, applications, and prospects. *J. Mater. Chem. A* **2020**, *8*, 6434−6470.
(57) Karatayeva, U.; Siyabi, S. A. A.; Narzary, B. B.; Baker, B. C.; Faul, C. F. J. Conjugated Microporous Polymers for Catalytic CO_2 Conversion. *Adv. Sci.* **2024**, *11*, No. 2308228.
(58) Hsiao, C. W.; Elewa, A. M.; Mohamed, M. G.; Kuo, S. W. Highly stable hybrid porous polymers containing polyhedral oligomeric silsesquioxane (POSS)/Dibenzo[g,p]chrysene and Dibenzo[b,d]thiophene units for efficient Rhodamine B dye removal. *Sep. Purif. Technol.* **2024**, *332*, No. 125771.
(59) Mohamed, M. G.; Hu, H. Y.; Santhoshkumar, S.; Madhu, M.; Mansoure, T. H.; Hsiao, C. W.; Ye, Y. S.; Huang, C. W.; Tseng, W. L.; Kuo, S. W. Design and synthesis of bifunctional conjugated microporous polymers containing tetraphenylethene and bisulfone units for energy storage and fluorescent sensing of p-nitrophenol. *Colloids Surf., A* **2024**, *680*, No. 132675.
(60) Mousa, A. O.; Mohamed, M. G.; Lin, Z. I.; Chuang, C. H.; Chen, C. K.; Kuo, S. W. Conjugated microporous polymers as a novel generation of drug carriers: A systemic study toward efficient carriers of tetracycline antibiotic. *Eur. Polym. J.* **2023**, *196*, No. 112254.
(61) Kong, X.; Zhou, S.; Strømme, M.; Xu, C. Redox active covalent organic framework-based conductive nanofibers for flexible energy storage device. *Carbon* **2021**, *171*, 248−256.
(62) Luo, B.; Chen, Y.; Zhang, Y.; Huo, J. Nitrogen-rich anthraquinone−triazine conjugated microporous polymer networks as high-performance supercapacitor. *New J. Chem.* **2021**, *45*, 17278−17286.
(63) Samy, M. M.; Mohamed, M. G.; Sharma, S. U.; Chaganti, S. V.; Lee, J. T.; Kuo, S. W. An Ultrastable Tetrabenzonaphthalene-Linked conjugated microporous polymer functioning as a high-performance electrode for supercapacitors. *J. Taiwan Inst. Chem. Eng.* **2024**, *158*, No. 104750.
(64) Chang, S. Y.; Elewa, A. M.; Mohamed, M. G.; Mekhemer, I. M. A.; Samy, M. M.; Zhang, K.; Chou, H. H.; Kuo, S. W. Rational design and synthesis of bifunctional Dibenzo[g,p]chrysene-based conjugated microporous polymers for energy storage and visible light-driven photocatalytic hydrogen evolution. *Mater. Today Chem.* **2023**, *33*, No. 101680.
(65) Mohamed, M. G.; Sharma, S. U.; Yang, C. H.; Samy, M. M.; Mohammed, A. A. K.; Chaganti, S. V.; Lee, J. T.; Kuo, S. W. Anthraquinone-Enriched Conjugated Microporous Polymers as Organic Cathode Materials for High-Performance Lithium-Ion Batteries. *ACS Appl. Energy Mater.* **2021**, *4*, 14628−14639.
(66) Mohamed, M. G.; Elewa, A. M.; Li, M. S.; Kuo, S. W. Construction and multifunctional of hypercrosslinked porous organic polymers containing ferrocene unit for high-performance iodine adsorption and supercapacitor. *J. Taiwan Inst. Chem. Eng.* **2023**, *150*, No. 105045.
(67) Mei, L.; Cui, X.; Wei, J.; Duan, Q.; Li, Y. Metal phthalocyanine-based conjugated microporous polymer/carbon nanotube composites as flexible electrodes for supercapacitors. *Dyes Pigm.* **2021**, *190*, No. 109299.
(68) Mei, L.; Wei, J. C.; Duan, Q. Construction of copper porphyrin-linked conjugated microporous polymer/carbon nanotube composite as flexible electrodes for supercapacitors. *J. Mater. Sci. Mater. Electron.* **2021**, *32*, 24953−24963.
(69) Samy, M. M.; Mohamed, M. G.; EL-Mahdy, A. F. M.; Mansoure, T. H.; Wu, K. C. W.; Kuo, S. W. High-Performance Supercapacitor Electrodes Prepared From Dispersions of Tetrabenzonaphthalene-Based Conjugated Microporous Polymers and Carbon Nanotubes. *ACS Appl. Mater. Interfaces* **2021**, *13*, 51906−51916.

https://doi.org/10.1021/acsaem.4c01276
ACS Appl. Energy Mater. 2024, 7, 5582−5593